Journal of Solid State Chemistry 181 (2008) 3121–3130

Contents lists available at ScienceDirect

Journal of Solid State Chemistry

journal homepage: www.elsevier.com/locate/jssc

Chemical bonding analysis and properties of $La_7Os_4C_9$—A new structure type containing C- and C_2-units as Os-coordinating ligands

Enkhtsetseg Dashjav, Yurii Prots, Guido Kreiner, Walter Schnelle, Frank R. Wagner *, Rüdiger Kniep

Max-Planck-Institut für Chemische Physik fester Stoffe, Nöthnitzer Straße 40, 01187 Dresden, Germany

ARTICLE INFO

Article history:
Received 28 May 2008
Received in revised form
29 July 2008
Accepted 3 August 2008
Available online 15 August 2008

Keywords:
Ternary carbides
Rare-earth metals
Transition metals
Crystal structure
Chemical bonding
ELI
ELF

ABSTRACT

The new ternary carbide $La_7Os_4C_9$ was prepared by argon arc-melting of the elements followed by subsequent heat treatment at 900 °C for 250 h. The compound crystallizes monoclinic, in the space group $C2/m$ ($a = 1198.5(2)$ pm, $b = 542.0(1)$ pm, $c = 1196.2(2)$ pm, $\beta = 111.04(1)°$, $V = 725.2(2) \times 10^6$ pm^3, $Z = 2$). The structure was determined from single crystal X-ray diffraction data and refined to a residual of $R_1 = 0.02$ ($wR_2 = 0.03$) for 4812 unique reflections and 64 variable parameters. Electrical resistivity and magnetic susceptibility measurements characterize the compound as a Pauli-paramagnetic metal. The crystal structure contains bridging C- and terminal C_2-units as Os-coordinating ligands, thereby forming polyanions $^1_\infty[Os_4(C_2)_2C_5]$ running along the [101] direction. The polyanions are composed of alternating $Os(C_2)C_2$ and OsC_3 units with the transition metal in distorted trigonal planar coordination. Charge compensation is ensured by La cations which are situated in-between the polyanions. The carbon–carbon bond (131 pm) within the C_2 pairs is slightly shorter than the value of a common C–C double bond, and is discussed on the basis of COHP curves on the one side, and with ELI-D and electron density distributions on the other side. The method of partial ELI-D decomposition is shown to be well suited for the characterization of separated DOS structures in terms of chemical bonding signatures provided by ELI-D. The Os–La interactions are shown to be of a polar multicenter-bonding type with Os playing the role of the electron donor. Compared to an acetylide the C_2 species were found to possess a significantly reduced bond order and an enhanced number of electrons in lone pair type spatial regions. This type of species cannot be simply classified in terms of model pictures such as C_2^{2-} and C_2^{4-}, respectively.

© 2008 Elsevier Inc. All rights reserved.

1. Introduction

In the recent past we started to investigate the chemistry of novel carbometalates. In the course of this research all the known ternary carbides $A_xT_yC_z$ (A = rare-earth metals and actinoids; T = transition metals) containing monoatomic species C^{4-} have been classified into the groups of carbometalates and metal-rich carbides [1]. In addition, ternary carbides containing C_2 units are also known, e.g., RE_2MnC_4 (RE = Y, Er, Tm) [2], $REFeC_2$ (RE = Y, Sm, Gd–Lu) [3], RE_2FeC_4 (RE = Y, Tb–Lu) [4], $RENiC_2$ (RE = Y, La–Nd, Sm, Gd–Ho) [5], $RECoC_2$ (RE = Y, La–Nd, Sm, Gd–Lu) [6], and Sc_3TC_4 (T = Fe, Co, Ni, Ru, Rh, Os, Ir) [7]. An example with C_3 units is $Sc_5Re_2C_7$ [8]. Furthermore, a number of ternary carbides, e.g., U_2NiC_3 [9], $La_2Ni_5C_3$ [10], $La_{12}Re_5C_{15}$ [11], $Er_{10}Ru_{10}C_{19}$ [12], and $U_2Cr_2C_5$ [13] containing C^{4-} and C_2^{4-} species as structural units have been reported. In the present paper we focus on the synthesis of $La_7Os_4C_9$, which can be seen as a new example for compounds with mixed carbon ligand types. So far, three structure types of osmium and rare-earth or actinoid metal ternary carbides are known: $Th_2[OsC_2]$ [14], $Y_2[OsC_2]$ [15] and $La_5Os_3C_{3.25}$ [16]. Their crystal structures exclusively contain monoatomic C^{4-} species as the coordinating ligands. It was already shown [1] that the first two compounds are classified as carbometalates whereas the latter phase represents a border case between carbometalates and metal-rich carbides. In the experimental part of the present contribution, we report on the synthesis, the crystal structure, some electronic properties (magnetism, electrical conductivity) of $La_7Os_4C_9$, and discuss the structural relationships to the known ternary osmium carbides.

On the theoretical side, recent methodological developments for the analysis of chemical bonding in position space, as initially applied—but by far not restricted—to molecules, now open a way to get deeper insight into complex bonding situations also for solids. The electron localization function (ELF) initially proposed by Becke and Edgecombe [17] for a Hartree-Fock wavefunction

* Corresponding author. Fax: +49 351 4646 3002.
E-mail addresses: wagner@cpfs.mpg.de (F.R. Wagner), kniep@cpfs.mpg.de (R. Kniep).

0022-4596/$ - see front matter © 2008 Elsevier Inc. All rights reserved.
doi:10.1016/j.jssc.2008.08.005

and later reinterpreted in the framework of density functional theory (DFT) by Savin et al. [18] is widely used for chemical bonding analysis [19]. Previously, an alternative derivation of what could be called the physical kernel of ELF has been presented [20]. In this functional named the electron localizability indicator (ELI) the physically unmotivated homogeneous electron gas reference of ELF has disappeared. Instead, a physically transparent procedure based on so-called ω-restricted space partitioning made it possible to consistently derive general expressions for ELI valid also for fully correlated wavefunctions [21], for unlike-spin electron pairs [22], for spin-polarized systems [23], and all that not only in position but also in momentum space [24]. In the case of a time-independent, monodeterminantal and non-spinpolarized wavefunction ELI simplifies to the relevant part of the ELF kernel [20,21,23,24b,25]. In this case, although still having different values, the topologies (positions and types of critical points, separatrices of basins) of ELF and ELI are strictly identical. The decisive advantage of usage of ELI instead of ELF is not only its general applicability as just mentioned, but also that for ELI a number of physically transparent tools for the analysis of a given ELI distribution are developed. Recently, based on a favorable ELI variant called ELI-D we have introduced the method of ELI-D decomposition into additive partial ELI-D (pELI-D) contributions from orbitals, which is not possible for ELF [25]. Exemplarily applied to molecules, this method is also applicable to solids, and it will be shown in the present investigation how it can be used. The above mentioned identical topologies of ELF and ELI in certain cases make it possible to reinvestigate ELF distributions obtained in these cases with the tools developed in the framework of ELI, provided the former are reinterpreted in the framework of ELI [25]. In the present investigation of the electronic structure an analysis of the transition metal–rare earth metal (*TM–RE*) interaction is made. It represents an exemplary analysis of an ELI-D *TM–RE* bonding feature we had noted earlier in our discussion of chemical bonding in the carbometalate $Pr_2[MoC_2]$ using ELF [26].

2. Experimental section

2.1. Preparation

The title compound was prepared by argon arc-melting of cold pressed pellets of the elements La (pieces, 99.99%, Alfa Aesar), Os (powder, 99.98%, Chempur) and C (graphite, powder, 99.95%, Chempur) with the nominal atomic ratio 7:4:9. Subsequently the samples were wrapped in Mo-foil, encapsulated in evacuated and fused silica ampoules, then annealed at 1173 K for 250 h, and finally quenched in water. The products are air and moisture sensitive and show a metallic luster. All preparations and handlings were carried out under argon in a glove box ($p(O_2, H_2O) <$ 1 ppm). No indication for decomposition or melting is observed by DTA measurements up to 1473 K in Nb crucibles under Ar atmosphere.

2.2. Phase analysis and crystal structure determination

For metallographic examination a piece of about 5 mm diameter was embedded in epoxy resin. Grinding was performed using fixed abrasive papers (SiC, grit sizes 45, 20 and 10 μm) and paraffin oil as lubricant. Polishing was done in four steps using a slurry of 6, 3, 1 and $\frac{1}{4}$ μm diamond powders in paraffin. After each step the specimens were cleaned with *n*-hexane to remove all particles and the paraffin oil. The microstructures of the annealed samples were examined by optical (bright light) and scanning electron microscopy (Zeiss Axioplan 2 and SEM Philips SL30). The metal content of the phases was determined by WDXS (Cameca SX 100, Os and $LaPd_2$ as standards).

Phase analysis and the determination of unit cell parameters were carried out by X-ray powder diffraction on the crushed and ground samples in the range $10^\circ < 2\theta < 110^\circ$ (Huber Guinier camera 670, Cu$K\alpha_1$ radiation, $\lambda = 154.059$ pm, transmission geometry, LaB_6 as an internal standard, $a = 415.692(1)$ pm). The sample was loaded between two *n*-hexane/vaseline coated Mylar foils in an aluminum cell. The title compound was found to be the majority phase besides a phase (< 5%) of unknown composition and structure. No perceptible homogeneity range was observed even by using variable carbon contents (±10%) during preparation. Observed and calculated X-ray powder patterns (after single-crystal structure refinement, see below) are shown in Fig. 1. The unit cell parameters were determined by least-squares refinement of the peak positions using the program "PPLP" [27].

Suitable single crystals of irregular shape were mounted on glass fibers and sealed in Lindemann glass capillaries. The intensity data were collected with a STOE-IPDS diffractometer with Ag$K\alpha$ radiation at room temperature. Relevant crystallographic data and details on data collection and structure refinement are given in Table 1.

2.3. Magnetization and electrical resistivity measurements

Magnetization measurements in external fields between 20 Oe and 70 kOe within the temperature range 1.8–400 K were performed on a SQUID magnetometer (MPMS XL-7, Quantum Design). The polycrystalline samples were sealed in quartz tubes under 0.4 bar He atmosphere. Corrections for the sample container were applied. The electrical resistance of the bulk sample used for the magnetic susceptibility was measured by a four point dc method between 4 and 320 K. The sample was handled under inert gas atmosphere. The estimated inaccuracy of the resistivity is ≈±30% due to the irregular geometry of the sample.

2.4. X-ray absorption spectroscopy (XAS)

The Os L_{III} XAS spectra of polycrystalline $La_7Os_4C_9$ were recorded in transmission geometry using synchrotron radiation (HASYLAB/DESY, Hamburg, E4 Beamline, Si(111) double-crystal monochromator). Due to the sensitivity against moisture and air, the samples were encapsulated in vacuum-tight stainless steel

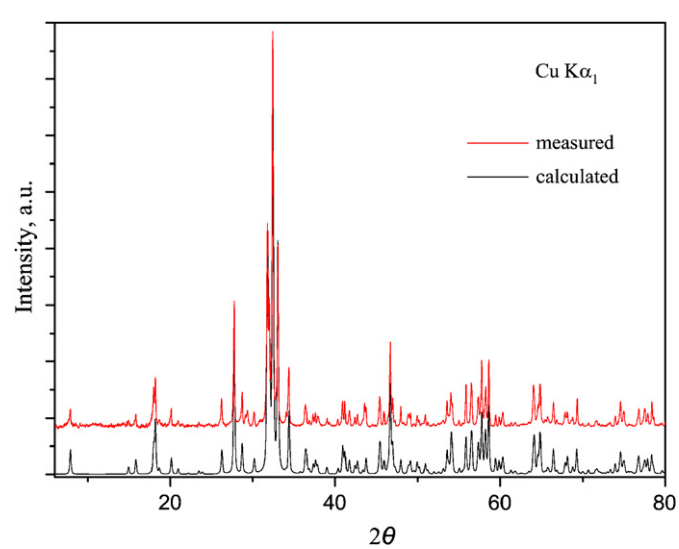

Fig. 1. Observed and calculated X-ray powder diffraction patterns of $La_7Os_4C_9$.

Table 1
Crystallographic data and details on data collection and structure refinement for $La_7Os_4C_9$

Chemical formula	$La_7Os_4C_9$
Formula mass ($g\,mol^{-1}$)	1841.38
Crystal system, space group, Z	Monoclinic, $C2/m$, 2
Radiation, λ (pm)	Ag$K\alpha$, 56.080
Temperature (K)	293(2)
a (pm)	1198.5(2)
b (pm)	542.0(1)
c (pm)	1196.2(2)
β (°)	111.04(1)
V ($pm^3 \times 10^6$)	725.2(2)
$\rho_{calc.}$ ($g\,cm^{-3}$)	8.433
T_{min}, T_{max}	0.7320, 1.0
Crystal size (mm^3)	$0.20 \times 0.10 \times 0.09$
Extinction coefficient x[a]	0.00061(2)
$R_{int.}$	0.0196
θ-range (deg)	2.7–40.0
hkl range	$-27 \leqslant h \leqslant 27$
	$-12 \leqslant k \leqslant 12$
	$-27 \leqslant l \leqslant 26$
Absorption correction	Multiscan
Absorption coefficient, μ (mm^{-1})	29.482
Refinement method	Full matrix least square on $\|F\|^2$
Unique reflections/parameters	4812/64
$R(F_o)/R_w(F_o^2)/GooF$ (all data)	0.020/0.027/1.29
max./min. $\Delta\rho$[e/($10^6\,pm^3$)]	2.66/−1.81
w1[b], w2[b]	0.001, 0

Supplementary data for this paper are available from the FIZ, D-76344 Eggenstein-Leopoldshafen, Germany, e-mail crysdata@FIZ-karlsruhe.de, by quoting the depository number 419389.

[a] F_c is multiplied by $k[1+0.001xF_c^2\lambda^3/\sin(2\theta)]^{-1/4}$

[b] $R = \Sigma\|F_o|-|F_c\|/\Sigma|F_o|$, $wR = \Sigma w(F_o^2-F_c^2)^2/(\Sigma w(F_o^2)^2)^{1/2}$ with $w = 1/[\sigma^2(F_o^2)+(w1P)^2+w2P]$ with $P = (\max(F_o^2,0)+2F_c^2)/3$.

containers sealed by In metal wires and equipped with Be windows of 0.5 mm thickness. Homogeneous absorbers were prepared by grinding the material together with dry B_4C powder.

2.5. Electronic structure calculations

The electronic structure was calculated from first principles using the self-consistent TB-LMTO-ASA method [28] within the local density approximation [29] of DFT. Atomic sphere and empty sphere radii were determined according to the automatic procedure proposed in Ref. [30]. Brillouin zone integrations were performed by an improved tetrahedron method using 1098 irreducible k-points from a total of 4096. The void space was filled with one empty sphere ES (wavefunction expansion center without nucleus) per primitive unit cell. The partial waves of La(6s, 5d, 4f), Os(6s, 6p, 5d), C(2s, 2p), and ES(1s) were explicitly included in the Hamiltonian, while those of La(6p), Os(4f), C(3d), and ES(2p) were treated according to a downfolding procedure.

Chemical bonding was examined within the framework of crystal orbital Hamilton population (COHP) analysis [31] (for the purpose of COHP calculations all the empty sphere orbitals have been downfolded as recommended [32]) and by analysis of the ELI [20]. The variant called ELI-D (Υ_D^α) offers novel ways to analyze given ELI-D distributions in terms of partial ELI-D contributions from orbitals ($\Upsilon_{D,i}^\alpha$) [25].

$$\Upsilon_D^\alpha(\boldsymbol{r}) = \rho_\alpha(\boldsymbol{r})\,\tilde{V}_D^\alpha(\boldsymbol{r}) = \sum_i^{\text{occ.}} \rho_{\alpha,i}(\boldsymbol{r})\,\tilde{V}_D^\alpha(\boldsymbol{r}) = \sum_i^{\text{occ}} \Upsilon_{D,i}^\alpha(\boldsymbol{r}). \quad (1)$$

The spin-resolved (e.g., α-spin) electron density ρ_α can be written as a sum of partial densities $\rho_{\alpha,i}$, e.g., from separate DOS regions, as is done in the present case. The pair-volume function $\tilde{V}_D^\alpha$ has to be calculated from all electrons, and for the time-independent, non spin-polarized, monodeterminantal wavefunction it is obtained from

$$\tilde{V}_D^\alpha(\boldsymbol{r}) = 12^{3/8}\left(\rho_\alpha(\boldsymbol{r})\sum_k \lambda_k \sum_i^{\text{occ.}\alpha} |\nabla\varphi_{i,k}(\boldsymbol{r})|^2 - \frac{1}{4}(\nabla\rho_\alpha(\boldsymbol{r}))^2\right)^{-3/8}, \quad (2)$$

where the spin-resolved crystal orbitals $\varphi_{i,k}$ with band index i and k-point index k are to be integrated over the 1st Brillouin zone, which is done by a discrete summation over selected k-points using k-point dependent weights λ_k. The band index has to be summed for all electrons up to the Fermi level.

The values of ELI-D are proportional to the charge (average number of same-spin electrons) needed to form a fixed fraction of a same-spin electron pair [24]. Moreover, they have been discussed in the framework of event probabilities to be proportional to the probability that the local charge (average number of same-spin electrons) is made from a single electron [24b]. From this fact it is obvious, that ELI-D is a measure of electron localizability. The physical meaning of an orbital's pELI-D contribution is that it monitors just the portion of charge a selected orbital contributes to the local total charge necessary to build a fixed fraction of a same-spin electron pair [25].

In contrast to ELF, where the values range between 0 and 1 due to an artificial Lorentzian type of scaling, the values of ELI-D are not scaled. They are limited to the interval between 0 and infinity. In chemical systems, ELI-D in the valence region only in exceptional cases (e.g., for H atoms, which have no core electrons) exceeds a value of 2.5 in regions with chemically significant electron density ($>10^{-4}\,bohr^{-3}$). In the present investigation partial ELI-D decomposition is applied to a crystalline compound for the first time in the literature.

3. Results and discussion

3.1. Crystal chemistry

Reflection conditions and Laue symmetry indicated the possible space groups $C2$, Cm, and $C2/m$. Lorentz-polarisation and absorption correction were applied using the program package 'CrystalClear' [33], and the crystal structure was solved and refined using the program packages SHELXS97 and SHELXL97 [34]. For the structure refinements the unit cell parameters from calibrated powder XRD data were used. The title compound crystallizes with space group $C2/m$ and a residual of $R_1 = 0.024$ ($wR_2 = 0.043$) for 6056 unique reflections and 64 variable parameters was obtained. Successive refinement of the various occupancy parameters provided no evidence for a deviation from the ideal composition $La_7Os_4C_9$, an observation which is in good agreement with the chemical composition determined from WDX: $La_{7.09(2)}Os_{3.99(1)}C_{8.91(1)}$. Positional and displacement parameters were standardized using the "Structure Tidy" program [35]. Relevant crystallographic data and details on data collection and structure refinement are given in Table 1. The fractional atomic coordinates, equivalent isotropic and anisotropic displacement parameters are listed in Tables 2 and 3, respectively.

The crystal structure of $La_7Os_4C_9$ represents a new structure type. Fig. 2 shows the crystal structure approximately viewed along [$\bar{1}$01]. The structure contains chains of polyanions $[Os_4(C_2)_2C_5]^{21-}$ running along [101] and La^{3+} ions in-between. Two types of carbon species, isolated C^{4-} (bridging) and C_2 pairs (terminal) can be clearly distinguished. Both are in a distorted octahedral coordination by metal atoms. The polyanions are composed of (OsC_3)- and ($Os(C_2)C_2$)-fragments with osmium in distorted trigonal planar coordination by carbon atoms as shown in Fig. 3. All monoatomic C^{4-} species serve as bridging ligands between Os atoms whereas the C_2 pairs occupy terminal

positions. There are two crystallographically independent Os atoms. Os1 has three monoatomic C^{4-} neighbors. Two of them form (Os_2C_4) fragments with an Os–Os distance of 272 pm (271 pm in the element) via the common edge (C1…C1). The Os2 atoms are surrounded by two C^{4-} and one end-on linked C_2 pair. The ($Os2(C_2)C_2$) units are again interconnected by monoatomic carbon. The C–C bond length within the C_2 pairs is 131 pm. This value is slightly shorter than the carbon–carbon double bond in ethene (133 pm). The Os–C distances vary between 192 and 207 pm, and are well comparable with the bond lengths of 209 pm in $Th_2[OsC_2]$ [14], 187–197 pm in $Y_2[OsC_2]$ [15] and 191 pm in $La_5Os_3C_{3.25}$ [16]. In these compounds the Os atoms exhibit low coordination numbers by monoatomic carbon, e.g., CN = 2 for $Th_2[OsC_2]$ and $La_5Os_3C_{3.25}$ or CN = 3 in $Y_2[OsC_2]$. The angles C–Os1–C inside the (OsC_3) unit range between 95.6° and 150.8° and the angles C–Os2–C in the ($Os(C_2)C_2$) unit between 114.9° and 125.8°. The La atoms are surrounded in a distorted square planar, tetrahedral and trigonal bipyramidal way by carbon i.e., with coordination numbers 4 and 5. The metal framework is shown in Fig. 4. The La atoms have 8, 10, 11 and 12 neighbors in form of distorted square prisms, bi-polar capped square prisms and distorted icosahedra, whereas Os atoms show mono- or three-capped trigonal prisms with CN of 7 and 9 as coordination type polyhedra. All interatomic distances are comparable to those found in the crystal structure of $La_5Os_3C_{3.25}$ [16]. Selected interatomic distances for $La_7Os_4C_9$ are listed in Table 4.

Table 2
Fractional atomic coordinates and equivalent isotropic displacement parameters [104 pm^2] ($U_{eq} = 1/3(U_{11}+U_{22}+U_{33})$; estimated standard deviations are given in parentheses)

Atom	Site	x	y	z	U_{eq}
La1	4i	0.12740(1)	$\frac{1}{2}$	0.84441(1)	0.00526(2)
La2	4i	0.36273(1)	$\frac{1}{2}$	0.38265(1)	0.00548(2)
La3	4i	0.64880(1)	$\frac{1}{2}$	0.32267(1)	0.00659(2)
La4	2a	0	0	0	0.00712(2)
Os1	4i	0.066574(6)	$\frac{1}{2}$	0.429005(6)	0.00433(1)
Os2	4i	0.142562(6)	$\frac{1}{2}$	0.141092(6)	0.00445(1)
C1	4i	0.1078(2)	$\frac{1}{2}$	0.6129(2)	0.0062(2)
C2	4i	0.1152(2)	$\frac{1}{2}$	0.2906(2)	0.0065(2)
C3	4i	0.3044(2)	$\frac{1}{2}$	0.1434(2)	0.0062(2)
C4	4i	0.4218(2)	$\frac{1}{2}$	0.1795(2)	0.0077(3)
C5	2b	0	$\frac{1}{2}$	0	0.0059(3)

Table 3
Anisotropic displacement parameters U_{ij}[104 pm^2] ($f_{T,\ anis} = \exp[-2\pi^2(U_{11}h^2a^{*2}+U_{22}k^2b^{*2}+U_{33}l^2c^{*2}+U_{12}hka^*b^*+U_{13}hla^*c^*+U_{23}klb^*c^*)]$ (estimated standard deviations are given in parentheses)

Atom	U_{11}	U_{22}	U_{33}	U_{13}	U_{23}	U_{12}
La1	0.00546(3)	0.00512(4)	0.00556(3)	0.00243(3)	0	0
La2	0.00567(3)	0.00512(4)	0.00496(3)	0.00109(3)	0	0
La3	0.00613(3)	0.00576(4)	0.00861(4)	0.00352(3)	0	0
La4	0.01018(5)	0.00530(5)	0.00655(5)	0.00382(4)	0	0
Os1	0.00474(2)	0.00500(2)	0.00358(2)	0.00190(2)	0	0
Os2	0.00374(2)	0.00628(3)	0.00331(2)	0.00124(2)	0	0
C1	0.0059(5)	0.0066(6)	0.0062(6)	0.0021(4)	0	0
C2	0.0079(6)	0.0064(6)	0.0057(6)	0.0029(5)	0	0
C3	0.0067(5)	0.0053(6)	0.0075(6)	0.0035(5)	0	0
C4	0.0063(6)	0.0075(7)	0.0094(6)	0.0030(5)	0	0
C5	0.0076(8)	0.0049(8)	0.0043(7)	0.0009(6)	0	0

3.2. Electronic structure

DOS projections for Os-, La- and C-orbitals are shown in Fig. 5. Below the Fermi level, which was set to 0 eV, the total DOS of the valence electrons displays five different structures denoted *A*1, *B*1, *A*2, *B*2, *C* with increasing energy. In the following they will be characterized, both, in Hilbert space on the basis of COHP diagrams (Fig. 6) and in position space on the basis of the electron density and partial ELI-D (pELI-D) contributions (Fig. 7). The orientation of the calculated slices is chosen similar to Fig. 3. The energetically lowest DOS structure *A1* (4e$^-$: $2 \times \sigma$ss) mainly represents the C–C σss bonds of the two C_2 units of the primitive unit cell. This can easily be seen from the *A1* partial electron density and the pELI-D contributions (Figs. 7a, b). Inspection of the C–C COHP diagram (Fig. 6) reveals that *A1* gives the major

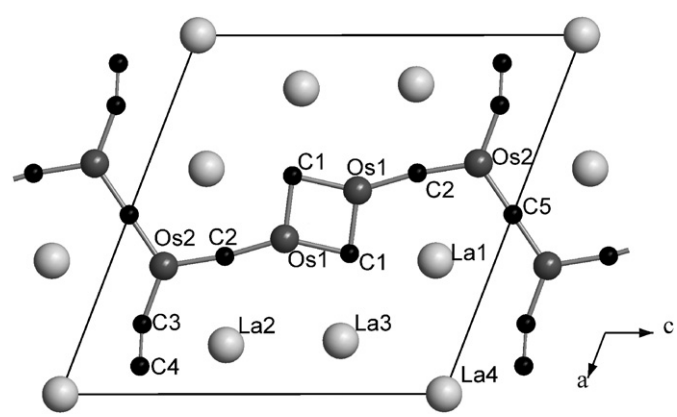

Fig. 3. View along [010] on a layer in the crystal structure of $La_7Os_4C_9$; for interatomic distances see Table 4.

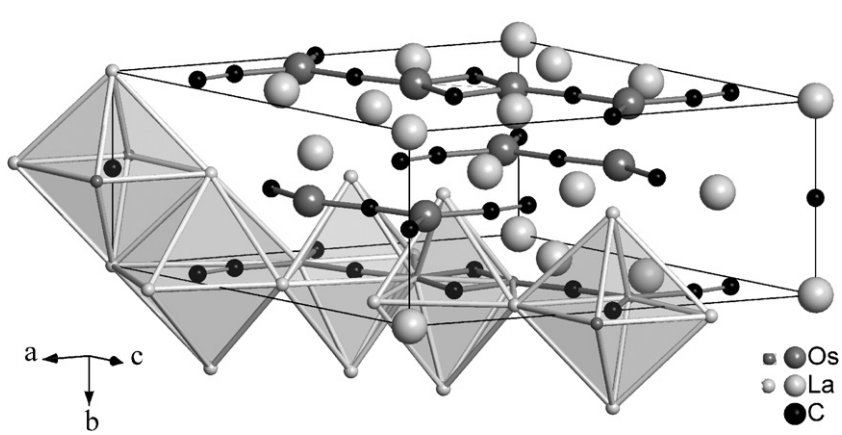

Fig. 2. View of the crystal structure of $La_7Os_4C_9$ approximately along [$\bar{1}$01] with coordination octahedra around selected carbon species (C, C_2).

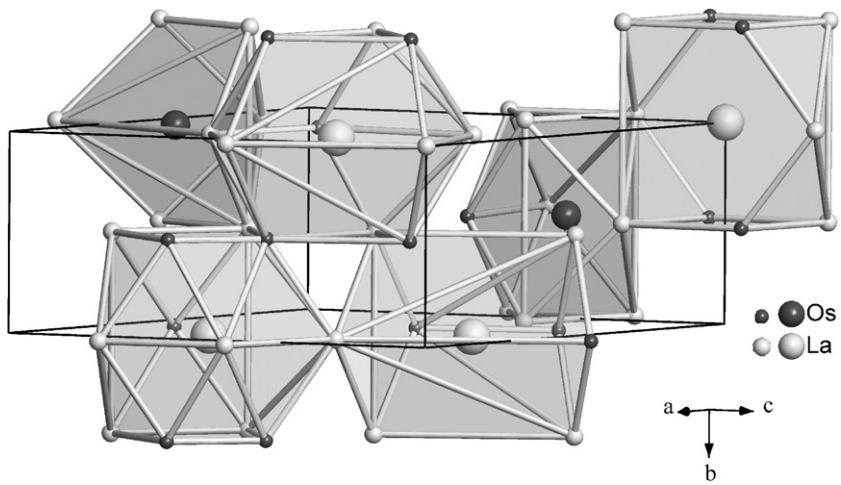

Fig. 4. Metal framework formed from La and Os and coordination polyhedra in the crystal structure of $La_7Os_4C_9$ (for further details see text).

Table 4
Integrated crystal orbital Hamilton populations (−ICOHP [eV/bond]) for selected interactions and distances (pm) for $La_7Os_4C_9$

Bond	n	Distance	−ICOHP	Bond	n	Distance	−ICOHP
Os1–C2	×4	194.3	6.64	Os1–Os1	×2	271.6	1.20
Os1–C1	×4	196.7	6.60			$-ICOHP_{aver.} = 1.20$	
Os1–C1	×4	207.4	4.59				
Os2–C5	×4	192.3	6.70	Os1–La1	×4	326.2	0.96
Os2–C3	×4	192.9	6.43	Os1–La3	×8	329.1	1.29
Os2–C2	×4	193.0	6.85	Os2–La2	×4	313.7	1.12
		$-ICOHP_{aver.} = 6.30$		Os2–La1	×4	330.2	0.87
La1–C1	×4	269.4	1.81	Os2–La4	×8	332.3	0.86
La1–C4	×8	276.6	1.39			$-ICOHP_{aver.} = 1.03$	
La1–C2	×4	277.3	1.55				
La1–C5	×4	279.9	1.38	La1–La2	×8	386.8	0.30
La1–C3	×8	281.9	1.04	La1–La3	×4	387.8	0.38
La2–C3	×4	269.1	1.21	La1–La4	×8	389.6	0.20
La2–C1	×8	273.1	1.44	La2–La2	×2	347.5	0.41
La2–C4	×4	276.4	1.17	La2–La3	×8	357.7	0.61
La2–C2	×4	276.9	1.34	La3–La2	×4	362.1	0.38
La3–C4	×4	264.3	2.09	La3–La4	×4	362.4	0.38
La3–C1	×4	273.6	1.47	La3–La2	×4	374.7	0.33
La3–C2	×8	274.6	1.18			$-ICOHP_{aver.} = 0.41$	
La4–C4	×4	263.3	1.72				
La4–C5	×4	271.0	1.24	C3–C4	×4	131.6	14.86
		$-ICOHP_{aver.} = 1.39$				$-ICOHP_{aver.} = 14.86$	

contributions to the integrated COHP (ICOHP(C–C)). From the substantially non-spherical shape of the partial electron density distribution around the C atoms quite substantial 2nd order mixing with the σpp orbital at higher energies can be inferred. The corresponding nominally antibonding σ^*ss combination is represented by structure *A*2 ($4e^-$: $2 \times \sigma^*$ss). The small antibonding COHP contributions already give a hint on the C–C nonbonding character of these bands. From the corresponding density and especially the pELI-D diagram (Figs. 7e, f) it becomes clear that these bands display mainly C–C lone pair type of character, since the pELI-D contributions reveal a characteristic topological feature on the bond-opposed side of the molecule, which persists in total ELI-D. It is pointing mainly to the Os atom and thus establishing a donor–acceptor type of interaction. In accordance with that, the corresponding COHP(Os–C_{pair}) diagram reveals bonding orbital interactions C–Os. Interestingly the other C atom of the C_2 unit, which is connected to a La atom instead, does not display this pELI-D feature here but at higher energies (structure *C*, see Figs. 7i, j), which is consistent with the smaller orbital interactions La–C (Fig. 6), as already discussed in previous works, e.g., [1].

DOS structures *B*1 and *B*2 mainly represent carbidic carbon contributions with some amount of electron density from the Os atoms. While *B*1 ($10e^-$: $5 \times C(2s^2)$) with smaller mixing of Os states mainly corresponds to the C(2s) densities of all the carbidic carbon species, *B*2 ($6e^-$: $3 \times C(2p^2)$) mainly consists of the trans-linearly coordinated carbide species displaying σp type interactions with Os atoms. This is corroborated from the partial density and pELI-D diagrams (Figs. 7c, d, g, h).

With $65e^-$ out of $89e^-$ the majority of valence electrons is contained in DOS structure *C*. Electronic book keeping reveals that by far not all carbon majority states have been attributed in the previous structures. Assuming formal C^{4-} units for the five isolated carbon species yields $(40–10–6)e^- = 24e^-$ to be contained in DOS structure *C*. As discussed in previous analyses of the electronic structure of rare earth transition metal carbides with isolated carbon atoms the La atoms can be assigned a formal charge according to La^{3+} [1]. Hence, the remaining $41e^-$ of DOS structure *C* are to be formally attributed to four Os atoms and two C_2 units. Taking into account that already $8e^-$ from DOS structures *A*1 and *A*2 have been attributed to the C_2 units there are still either $(20–8)e^-$ or $(24–8)e^-$ to be additionally attributed from DOS structure *C*, depending whether C_2^{2-} or C_2^{4-} is the appropriate notation of the actual C_2 species. Assigning the remaining $29e^-$ or $25e^-$ to four Os atoms, would then formally yield an $Os^{0.75+}$ or $Os^{1.75+}$ species, respectively. As expected from our previous analyses on rare earth carbometalates, in the corresponding COHP diagrams (Fig. 6) the electron-rich Os species is seen to be engaged in metal–metal bonds. According to COHP diagrams the majority of Os–Os interactions is produced in structures *B*1 and *B*2, where it occurs as a by-product of the carbon centered C–Os orbital interactions (see also Figs. 7c, d, g, h). In DOS region *C* where the Os majority states are located, no dominating contributions COHP(Os–Os) are found. This is consistent with the finding that the pELI-D distribution from region *C* does not show an attractor between the two carbon-bridged Os atoms (Fig. 7j). In contrast, for interactions Os–La DOS region *C* gives partial ELI-D contributions, which do display an attractor within a triangle of one Os and two La atoms (Fig. 7j). This feature survives in the total valence electron pELI-D (Fig. 8b) and is seen as a final feature also in total ELI-D (Fig. 8d). From a methodological point of view it is to be noted, that valence pELI-D represents a controllable approximation to (total) ELI-D in the valence region,

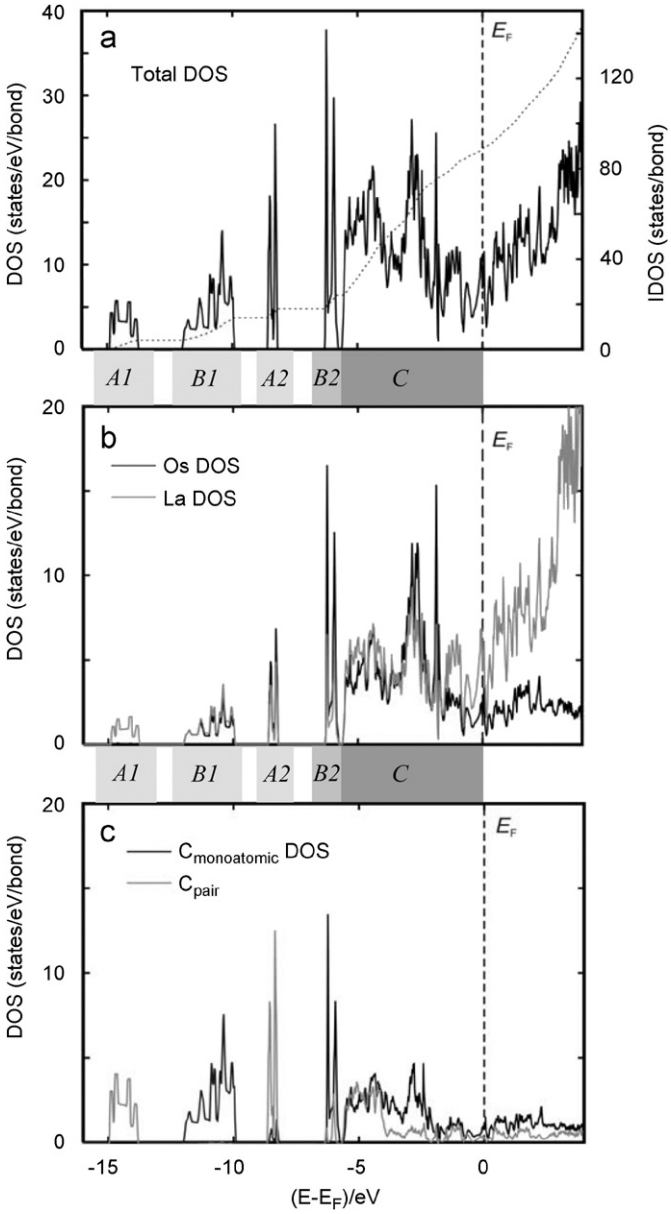

Fig. 5. Total DOS and atom-projected DOS for $La_7Os_4C_9$. Notation for DOS regions (*A*1, *B*1, *A*2, *B*2, *C*) is utilized in Fig. 7.

since the pELI-D core contributions are simply additive. This is in contrast to "valence ELF", where the "core ELF" contributions do not simply add to yield (total) ELF. Concerning the electron density it can be seen, that adding the partial densities to yield the valence density (Fig. 8a) already makes the interpretation in terms of chemical bonding less easy. Only for the C–C bond a pile up of valence charge density at the bond midpoint is observed. Inclusion of the core density to yield the physical electron density even removes this feature. Of course, the Laplacian of the electron density can be used to discuss chemical bonding, which is out of the scope of this contribution. A connection between the Laplacian of the density and ELI-D is discussed elsewhere [36].

The experimental verification of the existence of unsupported *TM–RE* two-center interactions has been recently reported for bimetallic metal-organic complexes $Cp_2Re–YCp_2$ and $Cp_2Re–YbCp_2$ (Cp = cyclo-C_5H_5) [37]. Based on the topological analysis of ELI-D and the electron density the bonding has been characterized as of donor–acceptor type [37]. As a quantitative measure of the *TM–RE* bond polarity the intersection between the ELI-D bond basin and the neighboring QTAIM (quantum theory of atoms-in-molecules [38]) basins of the electron density was built according to a proposal of Raub and Jansen [39b]. The basic idea behind is to choose the quantum mechanically defined mutually exclusive atomic regions in position space, i.e., the QTAIM basins of the electron density, as a means to physically partition the spatial region and the contained electronic population of a diatomic bonding ELI-D basin between two unlike bonding partners. Similar to findings for two-center early-late transition metal interactions [39a] for the *TM–RE* bonding situation it was shown that the ELI-D bond attractor is located well inside the QTAIM basin of the transition metal, which acts as the electron donor species [37]. More quantitatively, 84% of the electronic population of the ELI-D bonding basin (in total $0.8e^-$) was found to be contained in the QTAIM basin of the transition metal and only 14% in the QTAIM basin of the rare earth metal, which is an indication of a rather polar bonding situation [39b]. Performing the same kind of analysis for the compound under investigation yields similar results, but with two interesting extensions: (i) each of the two Os species forms this type of bonding interaction with La atoms twice along the [010] direction, and (ii) each of the two Os species significantly shares the ELI-D bonding basin with several La atoms yielding polycentric interactions Os–La. The observation of a multicenter *TM–RE* bonding ELF attractor has been already noted for the $Pr_2[MoC_2]$ model calculations [26]. For $La_7Os_4C_9$ a deeper analysis of the bonding scenario is now possible. From the above charge decomposition of ELI-D it is already obvious, that the energetically highest DOS region *C* is mainly responsible for this kind of bonding interaction. Furthermore, denoting the Os–La bonding basins according to the "donating" Os species it is found that the Os1 donor basin is significantly shared with five La atoms, while the Os2 donor basin is significantly shared with three La atoms. Each Os atom is engaged in two identical donor-type interactions along [010]. This can be seen in Fig. 8e, where the blue colored Os1 donor basin has a symmetrical analogue below the depicted (101) plane, which represents a mirror plane.

Despite the different number of sharing La atoms, according to the above described intersection procedure both Os species possess 78% of the electronic population of the bonding basin. For the Os1 donor basin the five La atoms each possess between 3% and 6% of the basin population of $1.4e^-$ yielding 19% in total, for Os2 the three La atoms possess 6% of the basin population of $1.1e^-$ yielding 18% in total. Thus, comparing also with the bimetallic situation in $Cp_2Re–YCp_2$ [37], independent of the number of electrons contained in the donor basin the transition metal roughly keeps its portion of the electronic population constant even for varying numbers of intersecting La atoms in polycentric bonding situations.

The situation is depicted in Fig. 8e. The gray translucent surfaces encompass the QTAIM basin of two Os1 and two Os2 species. Only half of the corresponding basins is shown, since they are cut by a corresponding mirror plane. The intersection of four Os–La bonding basins with atomic QTAIM basins is depicted. The four blue surfaces encompass the portion of the respective Os–La bonding basin which is inside the corresponding Os atom, and the red surfaces encompass the portion of the respective Os–La bonding basin which is inside the chosen La atom. Only one La atom intersection is exemplarily shown in order to give an impression about the different portions of the ELI-D bonding basin included in the Os and the La atomic basins.

Coming back to the bonding situation in the C_2 unit it must be stated that a satisfactory classification of the C_2 species cannot be

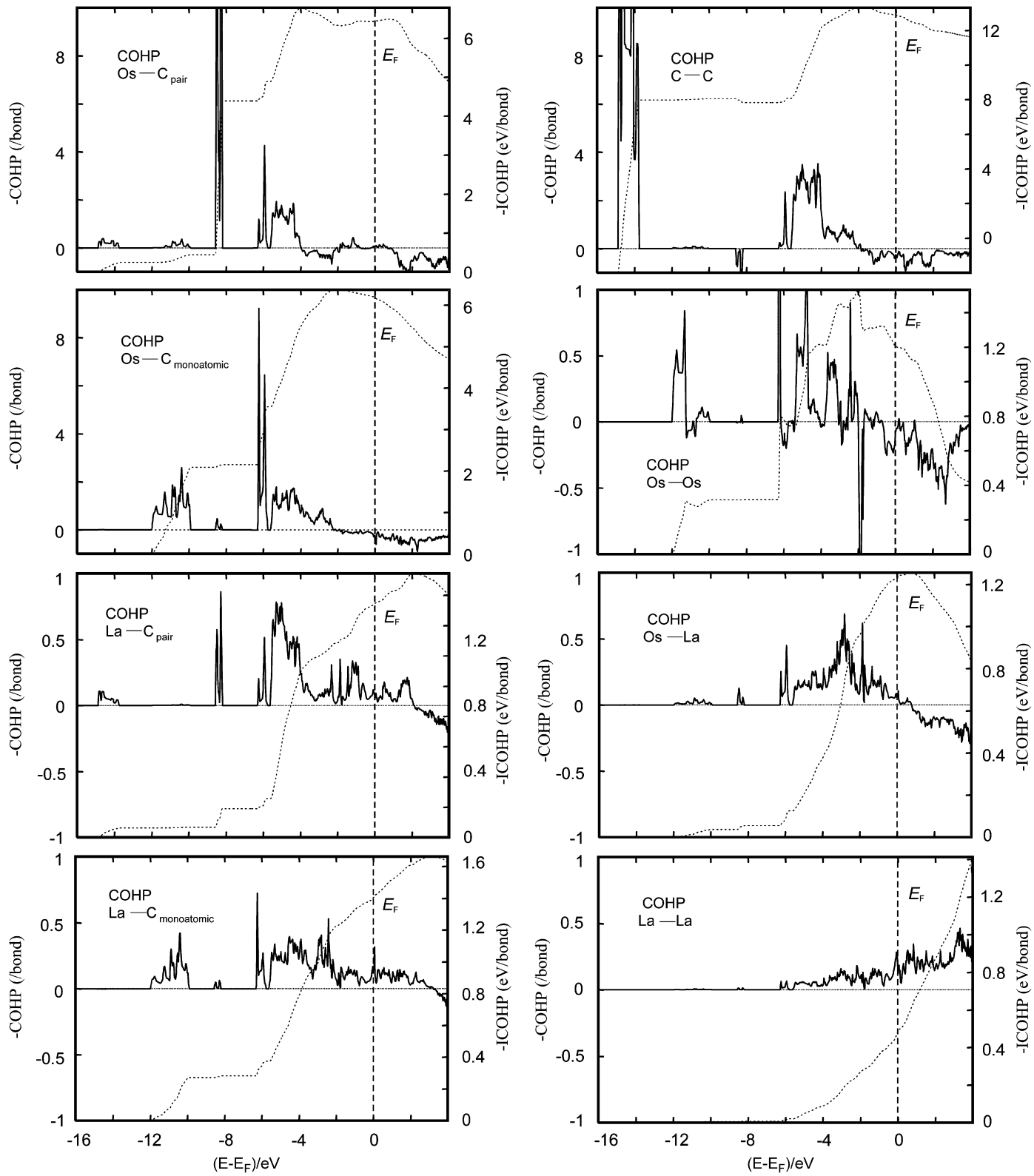

Fig. 6. COHP and integrated COHP (ICOHP) diagrams for metal–C interactions (left column), C–C and metal–metal interactions (right column) in the $La_7Os_4C_9$ crystal.

given. The reason is simply a lack of an established classification scheme, since the C_2 units are neither C_2^{2-} nor C_2^{4-} like, which is shown in the following.

In the isolated C_2^{2-} (isoelectronic to N_2) unit no antibonding π^* orbitals are occupied, while in the isolated C_2^{4-} (isoelectronic to O_2) half of the antibonding π^* orbitals are occupied. In both molecules the σp orbital is fully occupied, yielding formal bond orders of 3 and 2 for C_2^{2-} and C_2^{4-}, respectively. For the present compound COHP(C–C) curves for the σp and the two πp interactions indicate a roughly $\frac{3}{4}$ occupation of σ bonding levels and about $\frac{1}{10}$ population of antibonding π^* orbitals yielding a formal bond order of about 2.5.

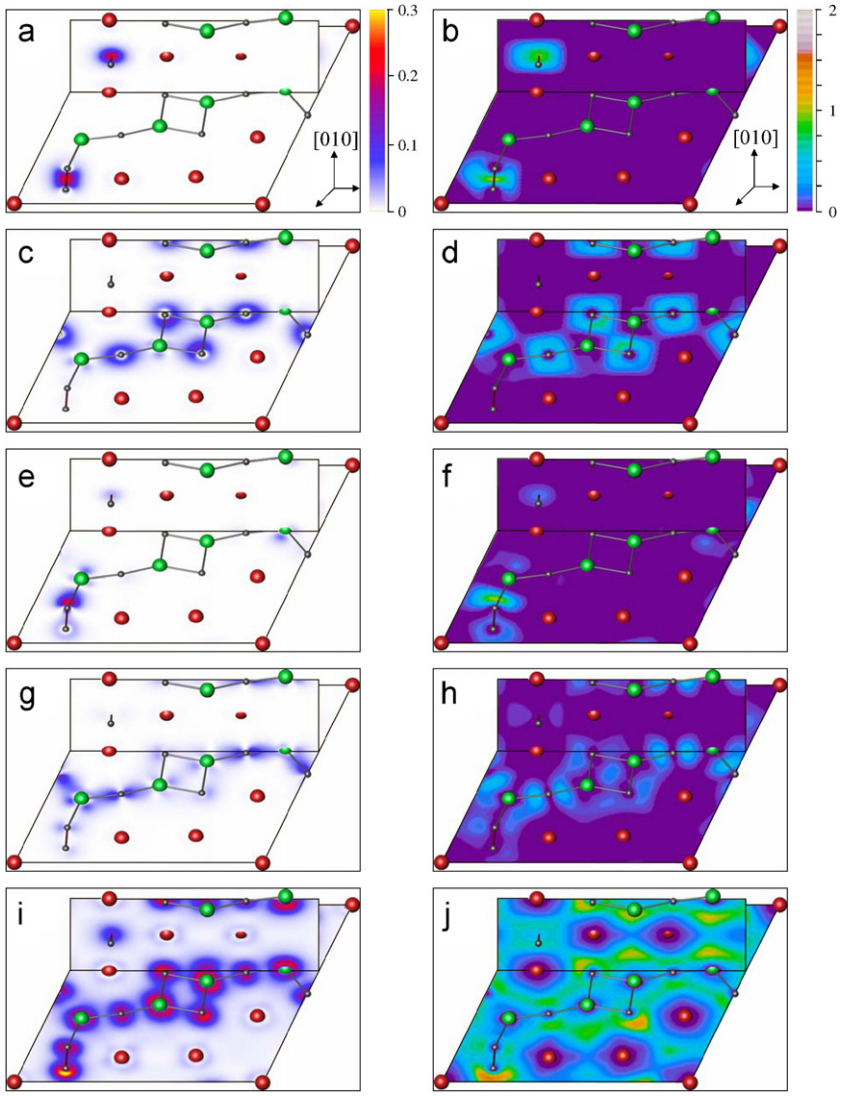

Fig. 7. Color-coded partial electron densities (left column) and corresponding pELI-D contributions (right column) for all valence DOS regions *A*1, *B*1, *A*2, *B*2, *C* (see Fig. 5). Colored spheres indicate La (red), Os (green) and C (gray) atoms.

In position space the following picture is obtained. The raw ELI-D (and ELF) disynaptic bond basin populations are not directly related to the formal bond order derived from the difference between the number of occupied bonding and antibonding MOs. It was shown, that usage of a suitable reference system may yield effective bond orders, which are consistent with interatomic force constants from lattice dynamical models fitted to experimental vibrational spectra [40]. We choose CaC_2 (tetragonal crystal structure from [41]) as the prototype compound for a C_2^{2-} unit. The total number of electrons for the C_2 unit in CaC_2 is calculated according to $2\times2.14e^-$ (C core)+$2\times3.14e^-$ (lone pair)+$3.25e^-$ (bond) $=13.8e^-$. The conceptually missing $0.2e^-$ are found in the Ca 3rd shell, which is a known chemical bonding effect. This shows that even for this quite ionic case, the electron counting for the C_2 unit using the ELI-D basin populations still misses part of the electrons compared to the formal electronic book keeping in the oxidation number procedure. Counting the total number of electrons for the present C_2 species according to $2\times2.13e^-$ (C core)+$2\times3.92e^-$ (lone pair)+$2.56e^-$ (bond) $=14.7e^-$ reveals an excess population of $0.9e^-$ over the reference C_2^{2-} unit. Even if one neglects that for participation of transition metal atoms a higher charge transfer into the metal's penultimate shell than in the CaC_2 case would not be unexpected, this result clearly rules out the C_2^{2-} scenario. Moreover, there are found $0.8e^-$ more in the lone pair type basins and $0.6e^-$ less in the bonding basin. Calculating a type of effective bond order from the ratio between the bond basin populations of the reference and the actual C_2 unit [40] yields $3\times2.56/3.25=2.4$, which is roughly the same as obtained from COHP analysis. Thus, although topologically there is only one lone pair type of attractor for each C atom of the C_2 species as in CaC_2, the present C_2 species displays an effective bond order between that of the C_2^{2-} and the C_2^{4-} unit. Based on all these findings a classification of the present C_2 units is not undertaken. Further systematic work on compounds containing C_2 units is necessary in order to establish a meaningful classification scheme. Therefore, at the present stage no formal charge assignment in the chemical formula is proposed.

3.3. Magnetization and electrical resistivity measurements

Magnetic susceptibility measurements on polycrystalline samples indicate a small amount of ferromagnetic impurities and a temperature independent paramagnetism of $\chi_0=+1.3\times10^{-3}$ emu mol^{-1} (Fig. 9). The magnetization of the samples in fields $H\leqslant1$ kOe displays a diamagnetic signal due to an unidentified superconducting phase with critical temperature $T_c\approx7.3$ K.

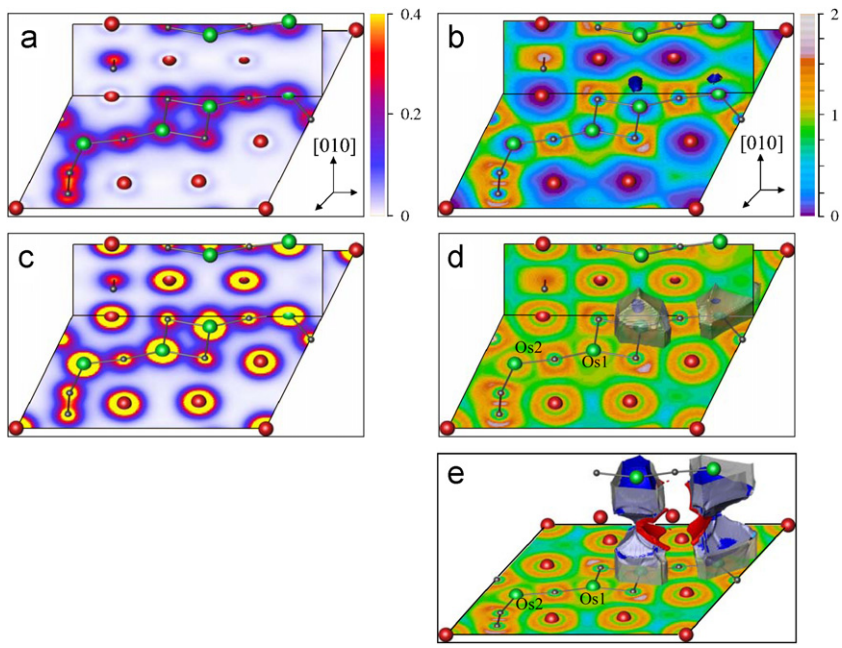

Fig. 8. Color-coded electron densities (left column) and ELI-D contributions (right column). Colored spheres indicate La (red), Os (green) and C (grey) atoms: (a) valence electron density; (b) valence electron pELI-D contributions; blue isosurface of pELI-D (at value 1.06) indicates Os–La bond attractor; (c) total electron density; (d) total ELI-D; blue isosurface of ELI-D (at value 1.07) indicates Os–La bond attractor; translucent surfaces display upper part of QTAIM basins of two Os atoms cut by the mirror plane; (e) total ELI-D; translucent surfaces display half of the QTAIM basins (cut by the corresponding mirror plane) of four Os atoms; blue bodies are completely contained within the corresponding QTAIM basin of an Os atom; each of them represents the intersection of a different Os–La bonding ELI-D basin with the QTAIM basin of the corresponding donor Os atom; red bodies represent the intersection of the Os–La bonding ELI-D basin with the QTAIM basin of one out of several attached La atoms.

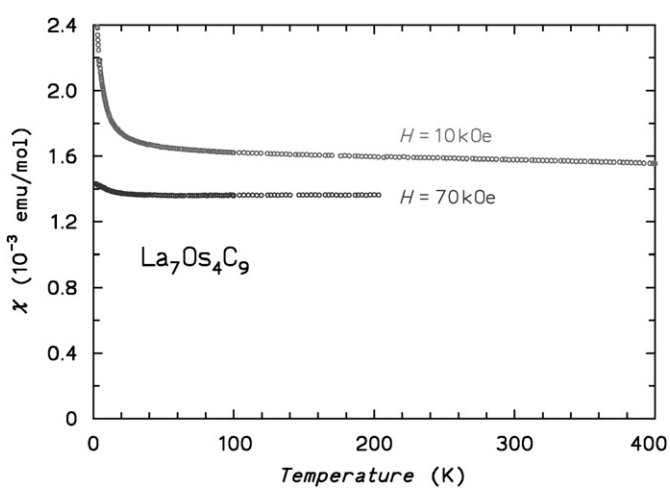

Fig. 9. Magnetic susceptibility $\chi = M/H$ versus temperature T for $La_7Os_4C_9$.

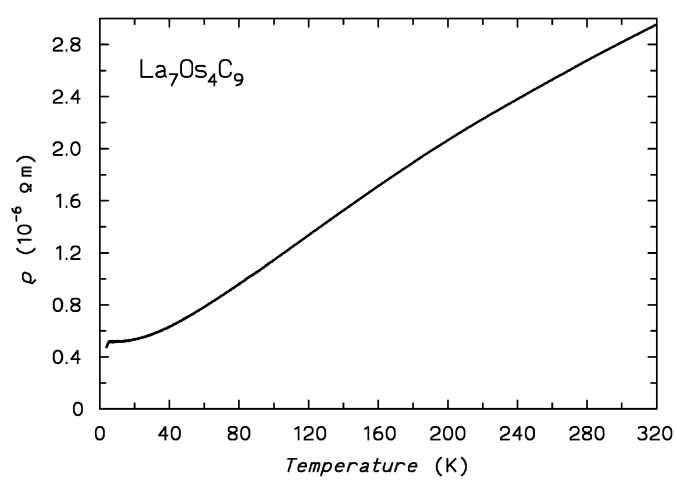

Fig. 10. Electrical resistivity ρ versus temperature T for $La_7Os_4C_9$.

The maximum relative phase volume estimated from the flux expulsion (shielding signal measured after zero-field cooling in $H = 20\,\mathrm{Oe}$) is about 0.5%, i.e. below the detection limit of X-ray powder diffraction.

The electrical resistivity $\rho(T)$ of $La_7Os_4C_9$ (Fig. 10) displays a temperature dependence typical for a metal. Together with the absolute resistivity values ($\rho_{300\,\mathrm{K}} \approx 280\,\mu\Omega\,\mathrm{cm}$, $\rho_0 \approx 50\,\mu\Omega\,\mathrm{cm}$) it can be concluded that $La_7Os_4C_9$ is a metal, in agreement with the electronic structure calculations (total DOS, Fig. 5a). A small but sharp decrease of $\rho(T)$ below 8 K is probably due to the superconducting secondary phase already seen in the magnetic susceptibility.

3.4. X-ray absorption spectroscopy (XAS)

For the comparison of the Os L_{III} absorption spectra of $La_7Os_4C_9$ the spectrum of $Y_2[OsC_2]$ was used as an Os(II) reference. As shown in Fig. 11 the spectra are very similar with respect to position and shape of the edges. Profile fitting of the Os L_{III} edge using a simple Gaussian and step function reveals that the absorption edges lie at same position for both compounds (within the resolution of 1 eV), namely, 10867 eV for $La_7Os_4C_9$ and 10868 eV for $Y_2[OsC_2]$, indicating similar oxidation states of Os in both compounds.

4. Conclusion

The crystal structure of the new ternary carbide $La_7Os_4C_9$ containing monoatomic C- as well as C_2-units as Os-coordinating ligands and representing a new structure type was determined by single crystal X-ray diffraction. The structure is composed of 1D covalent chains of $[Os_4(C_2)_2C_5]^{21-}$ running parallel along [101]

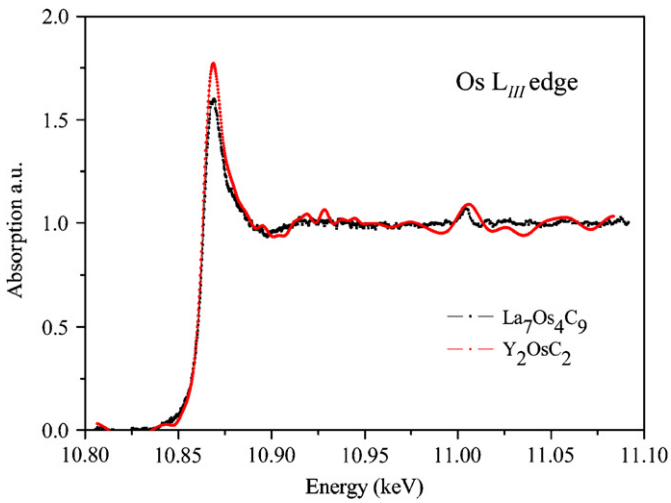

Fig. 11. XAS spectra of $La_7Os_4C_9$ and $Y_2[OsC_2]$ Os L_{III} threshold.

and La^{3+} ions in-between. The compound crystallizes monoclinic, in the space group $C2/m$ with the unit cell parameters $a = 1198.5(2)$ pm, $b = 542.0(1)$ pm, $c = 1196.2(2)$ pm, $\beta = 111.04(1)^\circ$, $V = 725.2(2) \times 10^6$ pm^3, and $Z = 2$. The distorted trigonal planar coordination around Os atoms by carbon is similar to that observed in the carboosmate(II) $Y_2[OsC_2]$. The charge decomposition analysis of ELI-D was applied for the first time to a solid yielding DOS decomposed partial ELI-D contributions. A comparison with COHP curves shows that—in analogy to their molecular analogues—they provide a bridge between the Hilbert space and the direct space representation of the chemical bond. As an extension to the highly polar bimetallic transition metal–rare earth metal donor–acceptor interaction discussed in the literature for metal-organic complexes the actual bonding situation Os–La is found to be of a multicenter bonding type with a roughly constant portion (for both Os species) of about 80% of the electrons in the ELI-D bonding basin being contained in the QTAIM basin of the Os atom. Each Os atom displays two such interactions along [010]. The electronic structure of the C_2 units has been characterized in detail using COHP on the one side, and ELI-D and the electron density on the other side. A decision in favor of either C_2^{2-} or C_2^{4-} has not been made due to the general lack of a qualified classification scheme at present. With the aid of the presented tools, this would be possible after corresponding data for a representative number of compounds containing C_2 units have been analyzed. Finally, we conclude that the title compound contains osmium with a low-oxidation state formally being between 0.75+ and 1.75+ according to the two border cases, $(La^{3+})_7\,(Os^{0.75+})_4\,(C^{4-})_5\,(C_2^{2-})_2$ and $(La^{3+})_7\,(Os^{1.75+})_4\,(C^{4-})_5\,(C_2^{2-})_2$.

Acknowledgments

We would like to thank Dr. U. Burkhardt, T. Vogel, M. Eckert (metallographic investigations and WDXS), Dr. H. Borrmann and S. Hückmann (X-ray diffraction). Funding by the Deutsche Forschungsgemeinschaft (SPP 1166) is gratefully acknowledged.

References

[1] E. Dashjav, G. Kreiner, W. Schnelle, F.R. Wagner, W. Jeitschko, R. Kniep, J. Solid State Chem. 180 (2007) 646–663.
[2] G.E. Kahnert, W. Jeitschko, G. Block, Z. Anorg. Allg. Chem. 619 (1993) 442–446.
[3] W. Jeitschko, M.H. Gerss, J. Less-Common Met. 116 (1986) 147–157.
[4] M.H. Gerss, W. Jeitschko, L. Boonk, J. Nientiedt, J. Grobe, J. Solid State Chem. 70 (1987) 19–28.
[5] H. Nowotny, E. Parthé, R. Kieffer, F. Benesovsky, Monatsh. Chem. 85 (1954) 255.
[6] H. Nowotny, R. Kieffer, F. Benesovsky, Rev. Metall. 55 (1958) 453.
[7] R.-D. Hoffmann, R. Pöttgen, W. Jeitschko, J. Solid State Chem. 99 (1992) 134–139.
[8] R. Pöttgen, W. Jeitschko, Z. Naturforsch. 47b (1992) 358.
[9] M.H. Gerss, W. Jeitschko, Z. Kristallogr. 175 (1986) 203.
[10] A.O. Tsokol, O.I. Bodak, E.P. Marusin, Sov. Phys. Crystallogr. 31 (1986) 39.
[11] G. Block, W. Jeitschko, Z. Kristallogr. 178 (1987) 25.
[12] R.-D. Hoffmann, W. Jeitschko, Z. Kristallogr. 178 (1987) 110.
[13] R.K. Behrens, W. Jeitschko, Z. Kristallogr. 182 (1988) 19.
[14] M.A. Moss, W. Jeitschko, Z. Anorg. Allg. Chem. 603 (1991) 57–67.
[15] M.H. Gerdes, W. Jeitschko, K.H. Wachtmann, M.E. Danebrock, J. Mater. Chem. 7 (1997) 2427–2431.
[16] K.H. Wachtmann, T. Hüfken, W. Jeitschko, J. Solid State Chem. 131 (1997) 49–53.
[17] A.D. Becke, K.E. Edgecombe, J. Chem. Phys. 92 (1990) 5397–5403.
[18] A. Savin, O. Jepsen, J. Flad, O.K. Andersen, H. Preuss, H.G. von Schnering, Angew. Chem. Int. Ed. 31 (1992) 187–188.
[19] C. Gatti, Z. Kristallogr. 220 (2005) 399–457.
[20] M. Kohout, Int. J. Quantum Chem. 97 (2004) 651–658.
[21] M. Kohout, K. Pernal, F.R. Wagner, Yu. Grin, Theor. Chem. Acc. 112 (2004) 453–459.
[22] M. Kohout, K. Pernal, F.R. Wagner, Yu. Grin, Theor. Chem. Acc. 113 (2005) 287–293.
[23] M. Kohout, F.R. Wagner, Yu. Grin, Theor. Chem. Acc. 119 (2008) 413–420.
[24] (a) M. Kohout, F.R. Wagner, Yu. Grin, Int. J. Quantum Chem. 106 (2006) 1499–1507;
(b) M. Kohout, Faraday Discuss 135 (2007) 43–54.
[25] F.R. Wagner, V. Bezugly, M. Kohout, Yu. Grin, Chem. Eur. J. 13 (2007) 5724–5741.
[26] E. Dashjav, G. Kreiner, W. Schnelle, F.R. Wagner, R. Kniep, Z. Anorg. Allg. Chem. 630 (2004) 689–696.
[27] E.J. Gabe, Y. Le Page, J.P. Charland, F.L. Lee, P.S. White, NRCVAX—An interactive program system for structure analysis, J. Appl. Crystallogr. 22 (1989) 384.
[28] O. Jepsen, A. Burkhard, O.K. Andersen, The Program TB-LMTO-ASA, version 4.7, Max-Planck-Institut für Festkörperforschung, Stuttgart, Germany, 1999.
[29] U. Barth, L. Hedin, J. Phys. C 5 (1972) 1629–1642.
[30] O. Jepsen, O.K. Andersen, Z. Phys. B 97 (1995) 35–47.
[31] R. Dronskowski, P.E. Blöchl, J. Phys. Chem. 97 (1993) 8617–8624.
[32] F. Boucher, O. Jepsen, O.K. Andersen, Supplement to the LMTO-ASA-Program Version 4.7, Stuttgart, Germany.
[33] Rigaku MSC, CrystalClear-Software, Version 1.3.6SP0, 2004.
[34] G.M. Sheldrick, SHELX97, Program for Crystal Structure, Refinement, University of Göttingen, Germany, 1997.
[35] L.M. Gelato, E. Parthé, J. Appl. Crystallogr. 20 (1987) 139–143.
[36] F.R. Wagner, M. Kohout, Yu. Grin, J. Phys. Chem. A (2008), in print.
[37] M.V. Butovskii, O.L. Tok, F.R. Wagner, R. Kempe, Angew. Chem. 120 (2008) 6569–6572;
Angew. Chem. Int. Ed. 47 (2008) 6469–6472.
[38] R.F.W. Bader, Atoms in Molecules: A Quantum Theory, Oxford University Press, Oxford, 1990.
[39] (a) G. Jansen, M. Schubart, B. Findeis, L.H. Gade, I.J. Scowen, M. McPartlin, J. Am. Chem. Soc. 120 (1998) 7239–7251;
(b) S. Raub, G. Jansen, Theor. Chem. Acc. 106 (2001) 223–232.
[40] S. Afyon, P. Höhn, M. Armbrüster, A. Baranov, F.R. Wagner, M. Somer, R. Kniep, Z. Anorg. Allg. Chem. 632 (2006) 1671–1680.
[41] J. Locher, F.H. Cocks, J. Mater. Sci. 15 (1980) 2520–2522.